Harnessing Optical Vortex Lattices in Nematic Liquid Crystals

R. Barboza,[1,2] U. Bortolozzo,[1] G. Assanto,[2] E. Vidal-Henriquez,[3] M. G. Clerc,[3] and S. Residori[1]

[1]*INLN, Université de Nice-Sophia Antipolis, CNRS, 1361 Route des Lucioles, 06560 Valbonne, France*

[2]*NooEL-Nonlinear Optics and OptoElectronics Lab, University Roma Tre, Via della Vasca Navale 84, 00146 Rome, Italy*

[3]*Departamento de Física, FCFM, Universidad de Chile, Casilla 487-3 Santiago, Chile*

(Received 14 June 2013; published 26 August 2013)

By creating self-induced vortexlike defects in the nematic liquid crystal layer of a light valve, we demonstrate the realization of programable lattices of optical vortices with arbitrary distribution in space. On each lattice site, every matter vortex acts as a photonic spin-to-orbital momentum coupler and an array of circularly polarized input beams is converted into an output array of vortex beams with topological charges consistent with the matter lattice. The vortex arrangements are explained on the basis of light-induced matter defects of both signs and consistent topological rules.

DOI: 10.1103/PhysRevLett.111.093902 PACS numbers: 42.25.−p, 42.50.Tx, 42.70.Df, 42.70.Gi

Optical vortices are singular points where the electromagnetic field goes to zero and around which the phase forms an n-armed spiral profile, with n the topological charge [1–3]. In low-order Gauss-Laguerre beams, a single optical vortex corresponds to a phase singularity on the axis of the beam. Vortex beams attract a lot of attention in view of their applications [4], including the exchange of angular momentum between light and matter [5], optical tweezers [6–8], quantum computation [9], data transmission [10], and enhancement of astronomical images [11]. To date, optical vortices were generated mainly by using spiral phase plates [12] or diffractive elements [13,14]. The introduction of q plates, planar elements with a preset radial director orientation [15], as well as the exploitation of umbiliclike defects [16] in nematic liquid crystals has opened new promising avenues, these approaches providing both tunability and high efficiency. Direct optical trapping of liquid crystal defects, first reported in nematics [17] and then extended to other textures, as cholesterics and smectics [18], was also demonstrated. However, the alignment of the incoming beam with the ''vortex-making'' element remains critical in certain conditions, for instance, in the presence of atmospheric turbulence as required by coronagraph applications [19]. By exploiting reorientational nonlinearities in the nematic liquid crystal (LC) layer of a light valve, we have recently realized vortex beams that are self-induced, and hence, self-aligned with the impinging light beam [20]. In this Letter, we show that a similar approach can be successfully exploited to create closely packed lattices of optical vortices with arbitrary and reconfigurable geometric distributions. As long as LC reorientation occurs only in the illuminated areas (which happens for relatively low amplitudes of the voltage applied to the light valve), the vortices on adjacent lattice sites are independent from one another and all have the same sign. Conversely, when reorientation occurs in the whole liquid crystal layer (for increased applied voltages), all the vortices become tightly coupled together, leading to the spontaneous generation of defects with opposite signs in between adjacent lattice sites. The resulting vortex arrangements are consistent with simple topological conservation rules accounting for the reconnection of reorientation lines in the distorted nematic layer. Similar rules were recently reported in topological colloids, where particles of various shapes were introduced in a nematic host [21], as well as in nematic samples submitted to magnetic fields created by small magnets [22]. Remarkably, in our case, all the topological reconnections are reconfigurable, optically addressable, and tunable via the voltage applied to the light valve. Moreover, the induced defect lattices act as arrays of photonic spin-to-orbital angular momentum couplers with both signs of the topological charge.

The vortex induction process is schematically represented in Fig. 1(a). The liquid crystal light valve (LCLV) is filled with a nematic mixture exhibiting negative dielectric anisotropy $\Delta\varepsilon = \varepsilon_{\parallel} - \varepsilon_{\perp} < 0$. In such a valve, the transparent interfaces are treated in order to provide the homeotropic alignment of the liquid crystals, that is, with the nematic director (optic axis) perpendicular to the confining walls, one of which is a photoconductive $Bi_{12}SiO_{20}$ (BSO) slab. Owing to this photoconductive substrate, when the LCLV is illuminated by a Gaussian light beam, the effective voltage drop across the LC layer acquires a bell shaped profile, peaked in the center of the illuminated area and able to overcome the critical value of the Fréedericksz transition for which the molecules start to reorient owing to the torque exerted by the electric field [23]. As we employ a liquid crystal with $\Delta\varepsilon < 0$, the torque exerted along the short molecular axis is larger than that on the long axis; therefore, the molecules tend to (re)align perpendicularly to the electric field, leading to a 2π-degenerate reorientation and the formation of topological defects in the nematic texture [24]. Besides, the Gaussian profile of the incoming beam also produces a transverse component of the electric field, thus giving rise to an effective potential able to pin the topological defect close to the optical intensity peak [20,25].

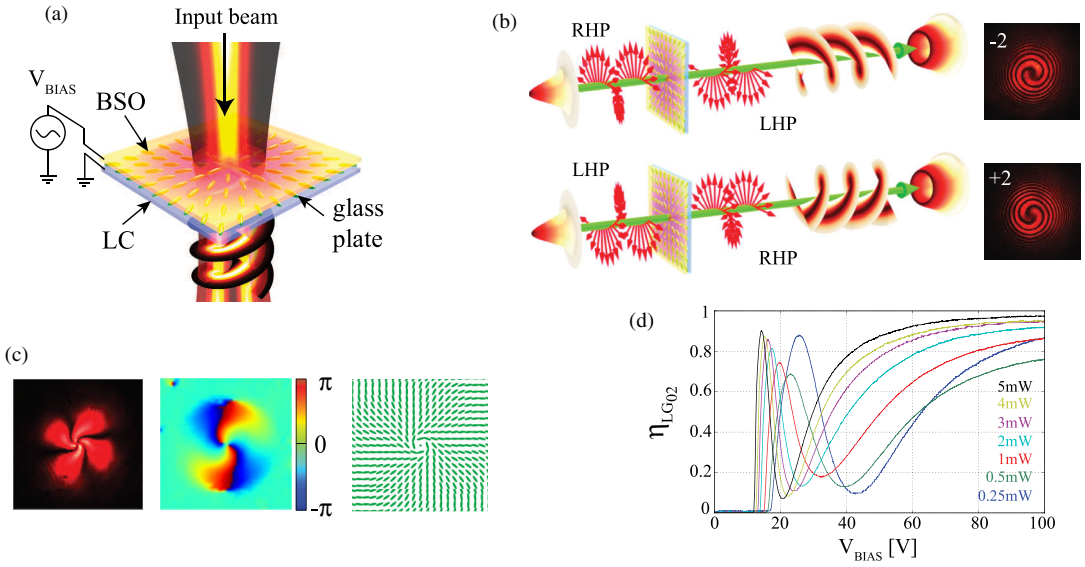

FIG. 1 (color online). Schematic representation of (a) optical vortex self-induction and (b) spin-to-orbital angular momentum transfer through the induced defect: An RHP (LHP) beam is converted into an LHP (RHP) beam with a phase singularity of charge -2 $(+2)$; experimental interferograms are shown beside the respective panels. (c) A matter defect observed under crossed polarizers (left); spatially resolved polarimetry (middle); reconstructed molecular organization (right). (d) Spin-to-orbital angular momentum conversion efficiency measured versus voltage bias and for various input intensities.

The created defect, in turn, couples orbital and spin components of the optical angular momentum; hence, the outgoing beam acquires a helical wavefront. The matter-defect–optical-vortex duality and their mutual coupling are illustrated in Fig. 1(b). An input Gaussian beam produces a vortexlike distribution of the LC molecules (a defect) and, because of the different phase retardations undergone by ordinary and extraordinary waves, a right-handed (left-handed) RHP (LHP) circularly polarized beam gets transformed into a Gauss-Laguerre beam of opposite polarization and carrying a phase singularity of topological charge -2 $(+2)$. Actual snapshots of output beams with spiraling interference fringes are shown beside the respective panels in Fig. 1(b). The opposite signs of the optical vortices are revealed by the opposite rotations of the spiral arms. The matter defect was initially characterized by observing it under crossed polarizers [left panel of Fig. 1(c)]. The black cross appearing in these conditions is the signature of a umbiliclike defect, which can be produced by two different types of deformations of the nematic texture, corresponding to ± 1 signs, or winding numbers, of the defect [26]. In order to discriminate the sign of the defect, we carried out spatially resolved polarimetry [27]: using quarter-wave plates, we analyzed the local birefringence and reconstructed the phase distribution around the defect [central panel of Fig. 1(c)]. The polarimetric profile shows that the defect is, indeed, umbiliclike and of winding number $q = +1$. Note that the reconstructed phase is proportional to 2θ, with θ the liquid crystal tilt in the transverse plane; therefore, the 4π phase jump around the singularity indicates a 2π change of the LC tilt angle θ. Correspondingly, the reconstructed molecular organization in the transverse plane has an azimuthal distribution [right panel of Fig. 1(c)]; hence, the defect acts as a q plate, to which a Jones matrix can be associated [28]. It can be shown that for a circularly polarized input $\vec{e}_\sigma = (\alpha/\sqrt{2})(\vec{x} + i\sigma\vec{y})$, where α is the amplitude and $\sigma = +1$ (-1) stands for the LHP (RHP), the exit field is given by $\vec{e}_{\rm out} = \alpha\cos(\delta/2)\vec{e}_\sigma + \exp(2iq\sigma\xi)$ $\alpha\exp(2i\sigma\theta_0)\sin(\delta/2)\vec{e}_{-\sigma}$; that is, the incoming circular polarization is converted to the opposite one with a helical phase $\exp 2iq\xi$ through a conversion factor $\sin^2(\delta/2)$, δ being the overall phase shift between ordinary and extraordinary components. The conversion efficiency, measured by recording the intensity of the output (converted) beam for different input powers, is plotted versus voltage bias in Fig. 1(d). For small input powers, the Fréedericksz threshold is large due to the voltage drop over the BSO slab. For higher powers, the vortex appears sooner due to the increased conductivity of the BSO. In each curve, the first peak is reached when δ is an odd multiple of π. Saturation occurs at high voltages.

In order to describe the mechanism of the optical vortex self-induction, we have derived from first principles a forced Ginzburg-Landau equation [25]

$$\gamma\partial_t A = \mu A - aA|A|^2 + K\nabla_\perp^2 A + \Delta K\partial_{\eta,\eta}\bar{A} + b\frac{E_r(r,z)}{z}E_z e^{i\theta}, \quad (1)$$

where A is the amplitude of the LC director field deformation, μ is the bifurcation parameter describing

the Fréedericksz transition, a is the saturation parameter, $b \equiv \Delta\varepsilon 2d/\pi$, E_z and E_r are the longitudinal, respectively, transverse electric fields, $\partial_\eta \equiv \partial_x + i\partial_y$ is the derivative on the transverse (x, y) plane, $\nabla_\perp \equiv \partial_{\eta,\bar{\eta}}$, z is the longitudinal coordinate, $K \equiv (K_1 + K_2)/2$, and $\Delta K \equiv (K_1 - K_2)/2$ accounts for the elastic anisotropy K_i, $i = \{1, 2, 3\}$ being the LC elastic constants. Without the last two terms, the above equation is the well-known Ginzburg-Landau equation, a prototype model widely employed to describe dissipative vortex dynamics [2]. The inclusion of the last two terms accounts for the elastic anisotropy of the LC and the effective electric potential induced by the light impinging on the photoconductor, which are responsible for the pinning of the matter vortex at the center of the illuminated areas [20].

The setup for generating vortex lattices is sketched in Fig. 2. The beam of a diode-pumped frequency-doubled solid-state (DPSS) laser at wavelength $\lambda = 532$ nm is expanded, collimated, and directed to a spatial light modulator (SLM). The SLM is computer driven by intensity masks (an example is shown in the inset, the lattice period is 0.5 mm, and the diameter of the vortex core is 1.2 μm) which, through a lens, are imaged onto the BSO side of the LCLV. The vortex beams at the LCLV output are recorded by a CCD camera. In order to observe the whole orientational structure inside the LC layer, the LCLV is also illuminated by white light and the transmitted field is imaged at the CCD plane. Polarizers and red filters discriminate the green vortex beams from the white light transmitted through the valve. A He-Ne laser at wavelength $\lambda = 632$ nm is used to realize an interferometer, through which the phase singularities are visualized by making the whole vortex lattice interfere with an expanded collimated beam.

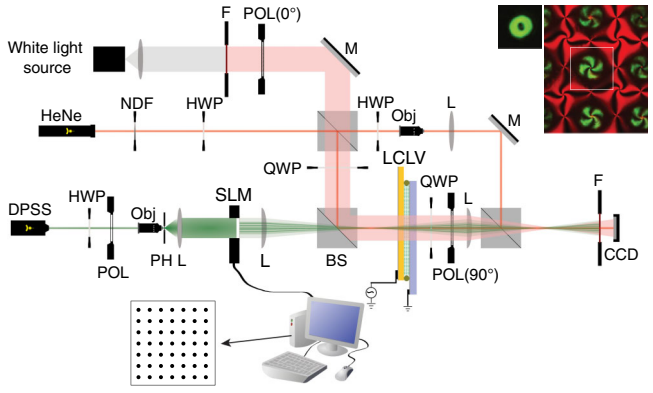

FIG. 2 (color online). Experimental setup. Obj, objective; BS, beam splitter; M, mirror; SLM, spatial light modulator; NDF, neutral density filter; F, filter transmitting the red components of the white light source for background illumination of the sample; POL, polarizer; HWP, half-wave plate; QWP, quarter-wave plate; PH, pinhole; L, lens; and CCD, charge-coupled device camera. Bottom inset: Example of square modulation mask as input to the SLM. Upper inset: Enlarged view of the sample observed under crossed polarizers when illuminated by the square grid (bright spots from the DPSS green laser) and white light background; on the left is an enlarged view of a single vortex.

Defect lattices were generated with various symmetries and spatial distributions, specifically designing the intensity masks for the SLM in order to achieve close packing of the vortices. Examples of hexagonal vortex lattices are displayed in Fig. 3. At low voltage, the vortices are independent from one another and can be individually addressed [Figs. 3(a) and 3(b)]. When the voltage is increased, adjacent vortices become coupled through reorientation in the whole nematic background. Because of the topological constraints associated with the reconnection of reorientation lines, two (initially generated) adjacent vortices of equal sign induce a vortex of opposite charge in between them. An example of fully connected network of vortices with alternating signs is visible in Fig. 3(c). Figure 3(d) presents the interferogram obtained with a plane reference wave. The spatially resolved polarimetry of the vortex distributions in Figs. 3(e) and 3(f) shows the

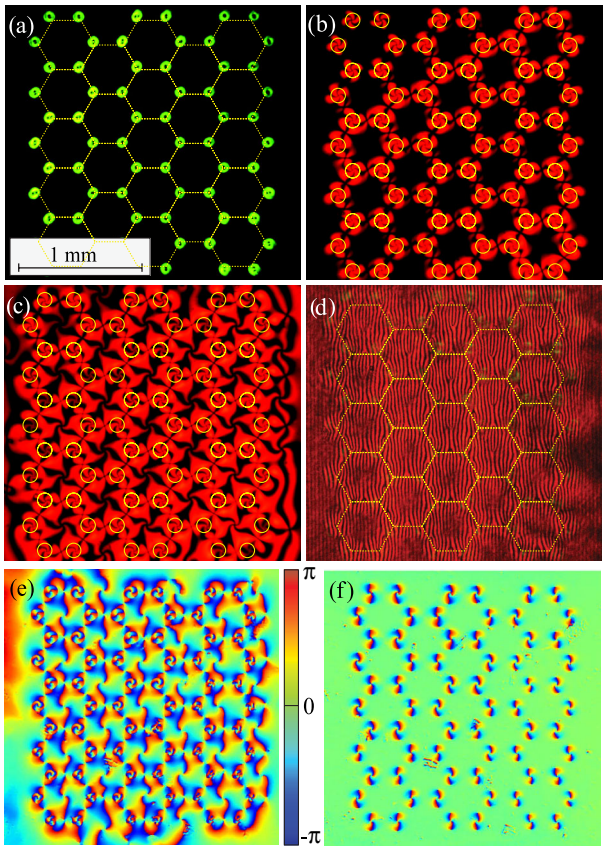

FIG. 3 (color online). Hexagonal vortex lattices: (a) Laser intensity distribution $V = 19$ V; (b),(c) white light images under crossed polarizers, (b) independent vortices $V = 18$ V and (c) fully coupled lattice $V = 22$ V; (d) interferogram $V = 12$ V; and (e),(f) spatially resolved polarimetry, (e) $V = 22$ V and (f) $V = 18$ V. The dashed lines mark the lattice structure, and the circles indicate the positions of the addressing light spots; the input intensity is $I = 250$ μW/cm^2.

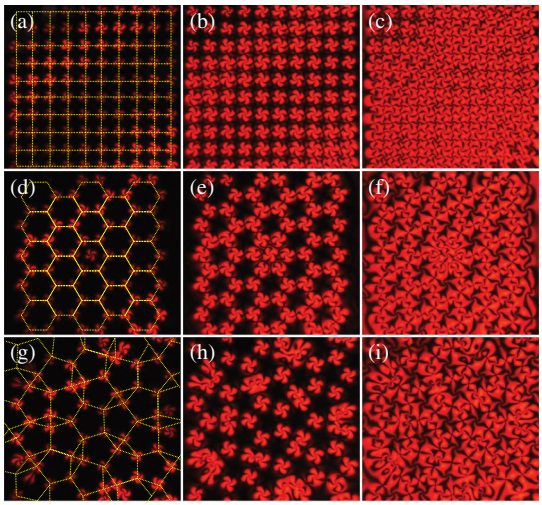

FIG. 4 (color online). Vortex lattices with various spatial distributions; the images were taken through crossed polarizers; input intensity $I = 250\ \mu\mathrm{W/cm^2}$. Squares for (a)–(c) $V = 14$, 18, 22 V, hexagons with a defect in the center for (d)–(f) $V = 14$, 18, 22 V, and Penrose lattice for (g)–(i) $V = 14$, 18, 22 V.

sign of each vortex by the direction of circulation of the phase arms.

Employing suitably designed intensity masks, we realized vortex lattices with various distributions. Figure 4 shows the cases of square, Penrose, and hexagonal lattices with a topological frustration in the center. Again, as the bias was increased from low to high voltages, we observed the transition from independent vortices to a fully connected network of adjacent vortices of alternating signs. In hexagonal lattices, a topological frustration is induced by addressing a defect in the center of a hexagonal cell. If this is done when the fully connected network is already established, the addressed defect undergoes a topological frustration with respect to the defect with opposite sign that was present at the same site. As a consequence, the unmatched reorientation lines reorganize themselves and give rise to a transient unwinding dynamics of the defect spiral arms, until the system is able to self-heal into a stationary configurational tradeoff [29].

Figures 5(a) and 5(b) display a numerical simulation of the vortex structure obtained by using the three-dimensional molecular director dynamics, illustrating, respectively, the molecular orientation around the defect core and the energy density of the associated deformation. Figure 5(c) shows the numerical solution of Eq. (1) [25]: the two initially addressed (by Gaussian beams) $q = +1$ vortices appearing in the middle of each illuminated area spontaneously induced an additional $q = -1$ vortex between them, owing to the topological constraints that force the reconnection of adjacent orientation lines in the nematic texture. These constraints could be exploited to establish the experimental induction of a $q = -1$ vortex, thereby demonstrating spin-to-orbital angular momentum

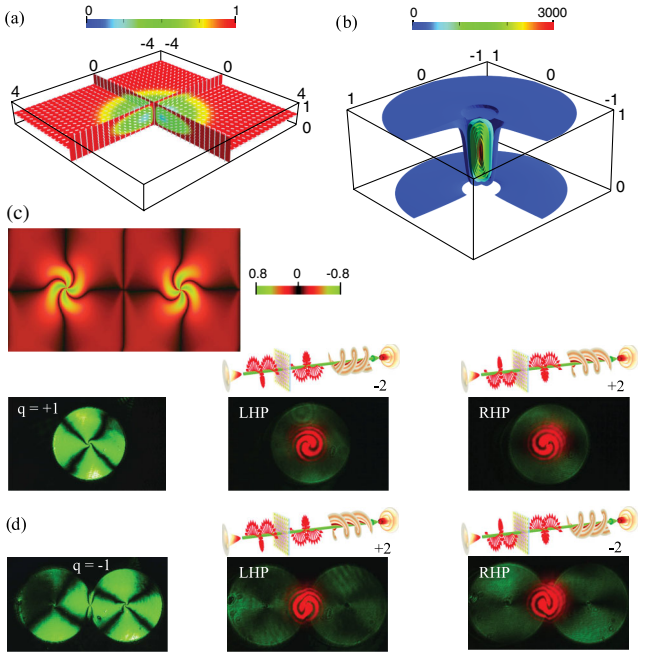

FIG. 5 (color online). Numerical distribution of (a) the molecular director and (b) energy density around the defect; lengths are normalized to the cell thickness. (c) Simulated vortex structure and spatial arrangement; two $+1$ vortices are initially addressed, with a -1 spontaneously appearing in between them. (d) Experimental demonstration of spin-to-orbital angular momentum transfer. Left panels: A $q = +1$ defect is created in the center of an illuminated area; a $q = -1$ defect is generated in between two spots. Central (right) panels: For an input LHP (RHP), the $q = +1$ defect yields an optical vortex with charge -2 $(+2)$, and the $q = -1$ defect produces an optical vortex with charge $+2$ (-2).

transfer for $q = \pm 1$ matter defects, as shown in Fig. 5(d) for individual lattice sites (the extension to all lattice sites is cumbersome but straightforward). A $q = +1$ defect is created in the center of an illuminated area, whereas a $q = -1$ defect is generated in between two adjacent illuminated spots. Correspondingly, for a LHP input, the $q = +1$ $(q = -1)$ defect produces an optical vortex of topological charge -2 $(+2)$; for a RHP input, the $q = +1$ $(q = -1)$ defect yields an optical vortex of charge $+2$ (-2). Noteworthily, manipulation and control of optical vortices can be achieved either by changing the polarization of the input beam or by employing matter defects with opposite signs.

In conclusion, we have shown that optical vortex lattices can be realized in a liquid crystal light valve. The optical vortices are driven by their counterparts in the nematic texture, where umbiliclike defects are created in closely packed configurations of various geometrical distributions. Every defect on each lattice site acts as a spin-to-orbital momentum coupler and can be harnessed either via optical addressing or by tuning the voltage applied to the light valve. These photonic structures, easily reconfigurable and

self-healing, can encompass the parallel processing of a large number of optical signals.

U. B., S. R., and M. G. C. acknowledge financial support from the ANR international program, Project No. ANR-2010-INTB-402-02 (ANR-CONICYT39), "COLORS," and FONDECYT No. 1120320. R. B. and G. A. acknowledge travel funding from the Internationalization Program of University Roma Tre.

[1] J. F. Nye and M. V. Berry, Proc. R. Soc. A **336**, 165 (1974).
[2] L. M. Pismen, *Vortices in Nonlinear Fields* (Oxford Science Publications, New York, 1999).
[3] M. S. Soskin and M. V. Vasnetov, Prog. Opt. **42**, 219 (2001).
[4] A. S. Desyatnikov, Y. S. Kivshar, and L. Torner, Prog. Opt. **47**, 291 (2005).
[5] L. Allen, M. W. Beijersbergen, R. J. C. Spreeuw, and J. P. Woerdman, Phys. Rev. A **45**, 8185 (1992).
[6] D. G. Grier, Nature (London) **424**, 810 (2003).
[7] V. G. Shvedov, A. V. Rode, Y. V. Izdebskaya, A. S. Desyatnikov, W. Krolikowski, and Y. S. Kivshar, Phys. Rev. Lett. **105**, 118103 (2010).
[8] M. Padgett and R. Bowman, Nat. Photonics **5**, 343 (2011).
[9] H. H. Arnaut and G. A. Barbosa, Phys. Rev. Lett. **85**, 286 (2000).
[10] J. Wang, J.-Y. Yang, I. M. Fazal, N. Ahmed, Y. Yan, H. Huang, Y. Ren, Y. Yue, S. Dolinar, M. Tur, and A. E. Willner, Nat. Photonics **6**, 488 (2012).
[11] F. Tamburini, G. Anzolin, G. Umbriaco, A. Bianchini, and C. Barbieri, Phys. Rev. Lett. **97**, 163903 (2006).
[12] M. W. Beijersbergen, L. Allen, H. E. L. O. van der Veen, and J. P. Woerdman, Opt. Commun. **96**, 123 (1993).
[13] V. Y. Bazhenov, M. V. Vasnetsov, and M. S. Soskin, JETP Lett. **52**, 429 (1990).
[14] Z. Sacks, D. Rozas, and G. A. Swartzlander, J. Opt. Soc. Am. B **15**, 2226 (1998).
[15] L. Marrucci, C. Manzo, and D. Paparo, Phys. Rev. Lett. **96**, 163905 (2006).
[16] E. Brasselet, Phys. Rev. Lett. **108**, 087801 (2012).
[17] J. Hotta, K. Sasaki, and H. Masuhara, Appl. Phys. Lett. **71**, 2085 (1997).
[18] I. I. Smalyukh, D. S. Kaputa, A. V. Kachynski, A. N. Kuzmin, and P. N. Prasad, Opt. Express **15**, 4359 (2007).
[19] E. Serabyn, D. Mawet, and R. Burruss, Nature (London) **464**, 1018 (2010).
[20] R. Barboza, U. Bortolozzo, G. Assanto, E. Vidal-Henriquez, M. G. Clerc, and S. Residori, Phys. Rev. Lett. **109**, 143901 (2012).
[21] B. Senyuk, Q. Liu, S. He, R. D. Kamien, R. B. Kusner, T. C. Lubensky, and I. I. Smalyukh, Nature (London) **493**, 200 (2012).
[22] P. Pieranski, B. Yang, L.-J. Burtz, A. Camu, and F. Simonetti, Liq. Cryst. **2012**, 1 (2012).
[23] P. G. de Gennes and J. Prost, *The Physics of Liquid Crystals* (Oxford Science Publications, New York, 1993), 2nd ed.
[24] R. Barboza, T. Sauma, U. Bortolozzo, G. Assanto, M. G. Clerc, and S. Residori, New J. Phys. **15**, 013028 (2013).
[25] See Supplemental Material at http://link.aps.org/supplemental/10.1103/PhysRevLett.111.093902 for the complete model derivation.
[26] S. Chandrasekhar, *Liquid Crystals* (Cambridge University Press, New York, 1977), p. 119.
[27] M. S. Soskin, V. G. Denisenko, and R. I. Egorov, Proc. SPIE Int. Soc. Opt. Eng. **5458**, 79 (2004).
[28] L. Marrucci, Mol. Cryst. Liq. Cryst. **488**, 148 (2008).
[29] See Supplemental Material at http://link.aps.org/supplemental/10.1103/PhysRevLett.111.093902 for a movie that shows an example of the unwinding dynamics of a defect under topological frustration.